

© 2019 by Akshat Puri. All rights reserved.

MEASUREMENT OF ANGULAR AND MOMENTUM DISTRIBUTIONS OF CHARGED
PARTICLES WITHIN AND AROUND JETS IN Pb+Pb AND $p\bar{p}$ COLLISIONS AT
 $\sqrt{S_{NN}} = 5.02$ TeV WITH ATLAS AT THE LHC

BY
AKSHAT PURI

DISSERTATION

Submitted in partial fulfillment of the requirements
for the degree of Doctor of Philosophy in Physics
in the Graduate College of the
University of Illinois at Urbana-Champaign, 2019

Urbana, Illinois

Doctoral Committee:

Professor Matthias Grosse Perdekamp, Chair
Professor Anne Marie Sickles, Advisor
¹ Professor Aida El-Khadra
Professor Bryce Gadaway

Abstract

² Studies of the fragmentation of jets into charged particles in heavy-ion collisions can help in understanding
³ the mechanism of jet quenching by the hot and dense matter created in such collisions, the quark-gluon
⁴ plasma. This thesis presents a measurement of the angular distribution of charged particles around the jet
⁵ axis as measured in Pb+Pb and pp collisions collided at a center of mass energy of $\sqrt{s_{NN}} = 5.02$ TeV. The
⁶ measurement is done using the ATLAS detector at the Large Hadron Collider, and utilizes 0.49 pb^{-1} of
⁷ Pb+Pb and 25 pb^{-1} of pp data collected in 2015. The measurement is performed for jets reconstructed
⁸ with the anti- k_t algorithm with radius parameter $R = 0.4$, and is extended to regions outside the jet cone.
⁹ Results are presented as a function of Pb+Pb collision centrality, and both jet and charged-particle transverse
¹⁰ momenta. It was observed that in Pb+Pb collisions there is a broadening of the jet for charged particles with
¹¹ $p_T < 4$ GeV, along with a narrowing for charged particles with $p_T > 4$ GeV. Ratios between the angular
¹² distributions in Pb+Pb and pp showed an enhancement for particles with $p_T < 4$ GeV in Pb+Pb collisions,
¹³ with the enhancement increasing up to 2 for $r < 0.3$, and remaining constant for $0.3 < r < 0.6$. Charged
¹⁴ particles with $p_T > 4$ GeV show a small enhancement in the jet core for $r < 0.05$, with a growing suppression
¹⁵ of up to 0.5 for $r < 0.3$ in Pb+Pb collisions. The depletion remains constant for $0.3 < r < 0.6$.

For my Mother, Father, and Brother

Contents

18	Chapter 1 Theoretical Introduction	1
19	1.1 Quantum Chromodynamics	1
20	1.2 Heavy Ion Collisions and the Quark Gluon Plasma	4
21	1.2.1 The Quark Gluon Plasma	5
22	1.3 Jets and Jet Quenching	6
23		

Chapter 1

Theoretical Introduction

This section shall discuss the theoretical background necessary to understand jet measurements. It is will discuss the fundamentals of quantum chromodynamics (QCD), the quark gluon plasma (QGP), jets, and subsequently jet energy loss.

1.1 Quantum Chromodynamics

The Standard Model (SM) [1] describes the interactions between elementary particles that are listed in Figure 1.1. It is one the most successful theories in physics and describes three of the four fundamental forces of nature. These are the strong interaction, the weak interaction, and the electromagnetic interaction. A quantum theory for gravity is not part of the SM.

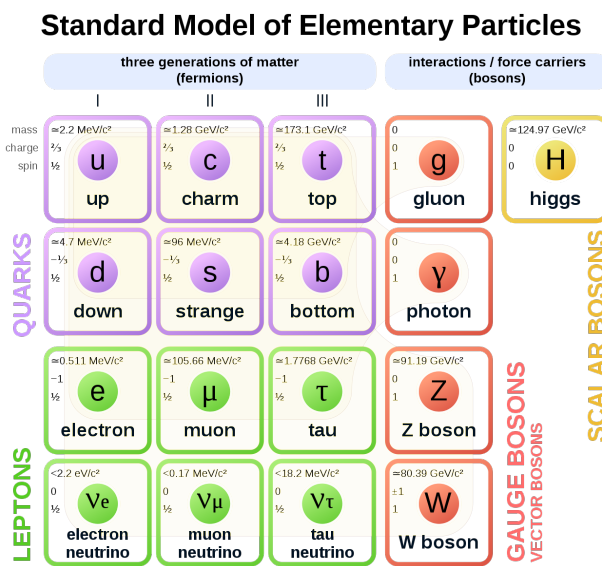


Figure 1.1: The elementary particles of the standard model.

Within the SM, the dynamics of the strong interactions involving quarks and gluons are described by

33 Quantum Chromodynamics (QCD), a gauge theory with SU(3) symmetry. Quarks are fermions with a spin
 34 of 1/2, and carry a fractional electric charge as well as a color charge. They all have mass and come in six
 35 flavors: up, down, top, bottom, strange, charm. The lightest quarks (u and d) combine and form stable
 36 particles, while the heavier quarks can only be produced in energetic environments and decay rapidly. Gluons
 37 are gauge bosons (force carriers) with a spin of 1, and are what hold quarks together. The dynamics of the
 38 quarks and gluons are described by the QCD Lagrangian given as [2]:

$$\mathcal{L}_{\text{QCD}} = \sum_q \bar{\psi}_{q,a} (i\gamma^\mu \partial_\mu \delta_{ab} - g_s \gamma^\mu t_{ab}^C \mathcal{A}_\mu^C - m_q \delta_{ab}) \psi_{q,b} - \frac{1}{4} F_{\mu\nu}^A F^{A\mu\nu} \quad (1.1)$$

39 where $\psi_{q,a}$ and $\psi_{q,b}$ are quark-filed spinors for a quarks with flavor q , mass m_q , and color a and b respectively,
 40 with the values for a and b ranging from 1 to 3 (for the three colors). The \mathcal{A}_μ^C corresponds to the gluon field
 41 with C taking values from 1 through 8 (for the 8 types of gluons). The t_{ab}^C corresponds to the Gell-Mann
 42 matrices that are the generators of the SU(3) group, and dictate the rotation of the quarks color in SU(3)
 43 space when it interacts with a gluon. The coupling constant is encoded within g_s , which is defined by
 44 $g_s \equiv \sqrt{4\pi\alpha_s}$. The field tensor $F_{\mu\nu}^A$ can be written in terms of the structure constants of the SU(3) group
 45 f_{ABC} , and is given by:

$$F_{\mu\nu}^A = \partial_\mu \mathcal{A}_\nu^A - \partial_\nu \mathcal{A}_\mu^A - g_s f_{ABC} \mathcal{A}^B \mathcal{A}^C \quad (1.2)$$

46 While many parallels can be drawn between Quantum Electrodynamics (QED) and QCD, the latter is a
 47 richer theory because its non-Abelian structure allows gluon-gluon interactions in addition to quark-gluon
 48 interactions. These interactions can be summarized as shown in Figure 1.2.

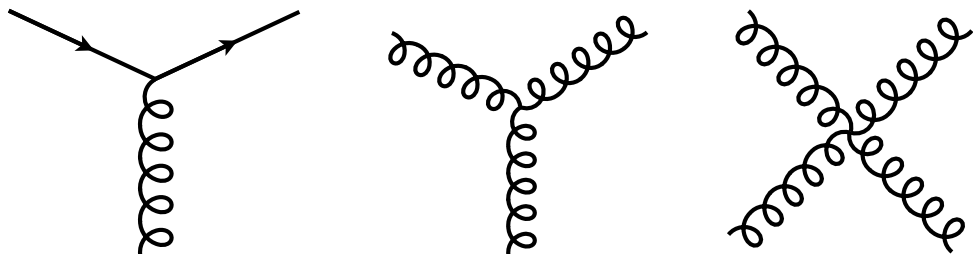


Figure 1.2: The allowed vertices in QCD. The vertices involving two or more gluons are unique to QCD and do not have a QED analog.

49 A core feature of QCD is that the coupling constant α_s has an energy dependence shown in Figure 1.3.

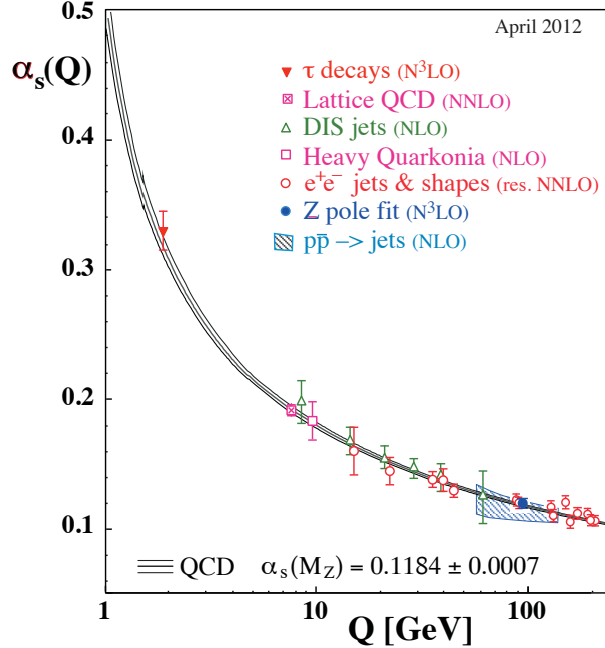


Figure 1.3: The running coupling constant α_s as a function of the momentum transfer Q . Figure taken from Ref. [2].

50 This dependence can be expressed in terms of the β function as

$$Q^2 \frac{\partial \alpha_s(Q^2)}{\partial Q^2} = \beta(\alpha_s(Q^2)) \quad (1.3)$$

51 where Q is the momentum transfer in the particle reaction. The beta function can be expressed using
52 perturbative QCD (pQCD) as

$$\beta(\alpha_s) = -(b_0 \alpha_s^2 + b_1 \alpha_s^3 + b_2 \alpha_s^4 \dots) \quad (1.4)$$

53 where the coefficients b_i depend on the number of colors and flavors.

54 This running coupling constant is small and asymptotically tends to zero at large energy scales (or at
55 small distances) and is large at small energy scales (large distances). This running coupling phenomenon
56 leads to two key behaviors: asymptotic freedom and color confinement.

57 **Asymptotic Freedom:** At high energy scales (small distances), the QCD coupling constant α_s is
58 small and tends to zero, implying a free particle behavior of quarks and gluons. This has been observed by a
59 variety of deep inelastic experiments [3–16]

60 **Color Confinement** The opposite end of the running coupling constant phenomenon is color confinement.
61 This property of QCD forbids the direct observation of free quarks and gluons, allowing only for
62 composite particles that are color singlets.

63 1.2 Heavy Ion Collisions and the Quark Gluon Plasma

64 In a heavy ion collision, each incident nucleus is a lorentz contracted disc. In the case of a Pb+Pb collision,
65 the nuclei have been accelerated to energies where the relativistic γ factor is between 100 and 2500 for beam
66 rapidities of $y = 5.3$ and 8.5 .

67 When these pancake like discs collide, most of the partons are participate in soft interactions that do not
68 involve large transverse momentum transfer, and are hence scattered only at small angles. A small fraction
69 of the colliding partons however do undergo hard perturbative interactions and lead to particles with large
70 transverse momenta.

71 While the maximum energy density in the process occurs just at the collision, the energy density $1 \text{ fm}/c$
72 after the collision is $12 \text{ GeV}/\text{fm}^3$, much higher than the $500 \text{ MeV}/\text{fm}^3$ in a typical hadron. Lattice QCD
73 calculations in thermodynamics show that at these energies, the partons produced in the collision cannot be
74 treated as a collection of distinct hadrons. In fact, these partons are strongly coupled to each other [??],
75 forming a medium that can be described by relativistic hydrodynamics. This medium, called the quark gluon
76 plasma (QGP) has a viscosity to entropy ratio that is almost at the theoretical minimum of $\eta/S = 1/4\pi$
77 [5, 6, check126].

78 After the collision and as the nuclei are receding from each other, the energy density between them
79 starts to decrease as the QGP cools and expands. This process can be seen in Figure 1.4. Once formed, the
80 QGP hydrodynamically flows, with the initial pressure driving the expansion and the subsequent cooling.
81 This continues till the energy density drops to below that within a hadron and the fluid hadronizes. These
82 individual hadrons briefly scatter off of each other before they freely fly towards the detector (freezeout).

83 While Figure 1.4 shows snapshots of a head on (central) collision between two large nuclei, it is possible to
84 have collisions where the impact parameter is larger and hence the overlap region is smaller. These collisions,
85 called peripheral collisions, qualitatively undergo the same process described above, with the size and shape
86 of the QGP being different. In these collisions, the QGP formed is more lenticular in the transverse direction.

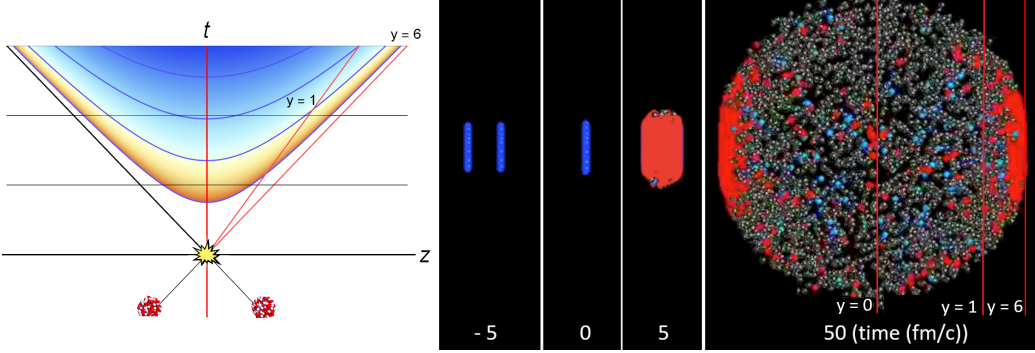


Figure 1.4: (left) Space-time diagram for a heavy ion collision. The color is indicative of the temperature of the QGP formed. (right) Snapshots of a heavy ion collision at $\sqrt{s_{\text{NN}}} = 2.76$ TeV at different times. The Lorentz contracted nuclei are in blue while the QGP is in red. Figures from References [7, 8].

- 87 Variations in the shape of the QGP due to the collision centrality result in pressure gradients that further
 88 cause azimuthal anisotropies in the momentum distribution of the produced particles.

89 **1.2.1 The Quark Gluon Plasma**

90 At the peak energy density of the collision, the system cannot be described at the level of hadrons, and has
 91 to be described in terms of quarks and gluons. The initial anisotropic energy density being reflected in the
 92 azimuthal variation of particle production implies a strongly coupled medium that expands hydrodynamically,
 93 with a faster expansion in the direction of larger gradients and hence resulting a momentum anisotropy. See
 94 [116, 117, 118, 63].

95 Azimuthal correlation measurements [5?, 6?, 90?, 110?, 111?] indicated the momentum anisotropy in
 96 the collision is remains, implying that the medium is strongly coupled.

97 A Fourier Transform of the angular distribution of charged hadrons in the collision debris can quantify
 98 these measurements and give the anisotropic flow coefficients v_n , defined as [115]:

$$\frac{d\bar{N}}{d\phi} = \frac{\bar{N}}{2\pi} \left(1 + 2 \sum_{n=1}^{\infty} v_n \cos(n(\phi - \bar{\Psi}_n)) \right) \quad (1.5)$$

99 where ϕ is the angle in the transverse plane, $\bar{\Psi}_n$ are the event plane angles, and \bar{N} is the average number
 100 of particles per event. Some of these coefficients are shown in Figure 1.5.

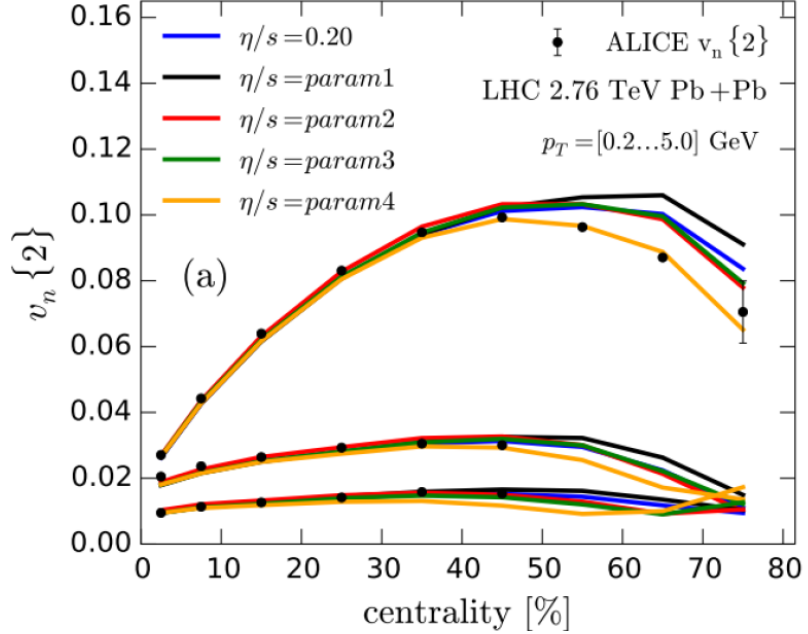


Figure 1.5: Comparison of a hydrodynamic model from [107] to the anisotropy measurements by ALICE [108] for different parameterizations of the η/s and for different $v_n(n = 2, 3, 4)$ from top to bottom as a function of collision centrality. – see ATLAS measurement from [109].

1.3 Jets and Jet Quenching

Hard scatterings in the colliding nuclei result in the production of highly energetic partons that evolve, decay, and eventually form conical sprays of particles called jets. Jet production is well understood in a pp collision environment (where there are no QGP effects) in the context of perturbative QCD [161]. In heavy ion collisions, jets must traverse the quark gluon plasma. This can result in the jet losing energy and forward momentum [162, 163], while also picking up momentum transverse to the parton direction. Jets can also deposit energy in the medium, creating a wake [71, 70].

Jet production shown in Figure 1.6 can be written in terms of the parton distribution functions, scattering cross sections, and the fragmentation functions as

$$d\sigma_{pp \rightarrow hX} \approx \sum_{abjd} \int dx_a \int dx_b \int dz_j f_{a/p}(x_a, \mu_f) \times f_{b/p}(x_b, \mu_f) \quad (1.6)$$

$$\times d\sigma_{ab \rightarrow jd}(\mu_f, \mu_F, \mu_R) \quad (1.7)$$

$$\times D_{j \rightarrow h}(Z_j, \mu_f) \quad (1.8)$$

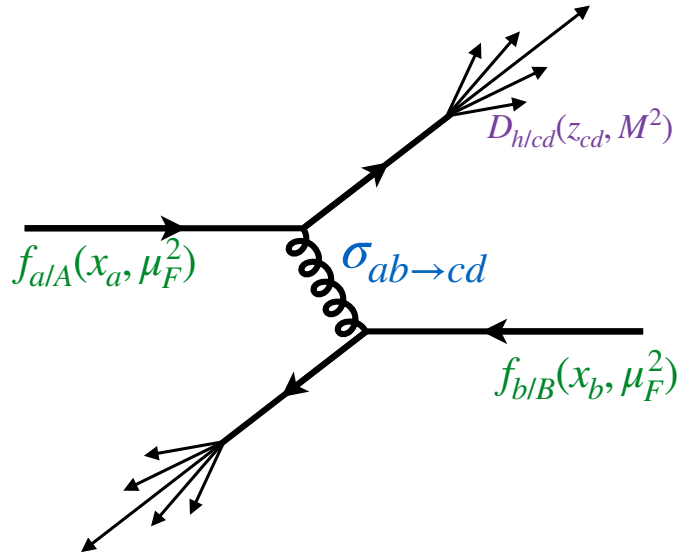


Figure 1.6: Jet production from the process $pp \rightarrow hX$, factorizing in terms of the parton distribution functions, scattering cross sections, and jet fragmentation functions. [[arXiv:1511.00790](https://arxiv.org/abs/1511.00790)]

110 These are discussed in Section 1.3.

Bibliography

- 111 [1] M. K. Gaillard, P. D. Grannis and F. J. Sciulli, *The Standard model of particle physics*, Rev. Mod.
112 Phys. **71** (1999) S96, arXiv: [hep-ph/9812285 \[hep-ph\]](#) (cit. on p. 1).
- 113 [2] J Beringer et al., *Review of Particle Physics, 2012-2013. Review of Particle Properties*, Phys. Rev. D
114 **86** (2012) 010001 (cit. on pp. 2, 3).
- 115 [3] A. Deur et al., *High precision determination of the Q^2 evolution of the Bjorken Sum*, Phys. Rev. D**90**
116 (2014) 012009, arXiv: [1405.7854 \[nucl-ex\]](#) (cit. on p. 4).
- 117 [4] J. H. Kim et al., *A Measurement of $\alpha_s(Q^2)$ from the Gross-Llewellyn Smith sum rule*, Phys. Rev. Lett.
118 **81** (1998) 3595, arXiv: [hep-ex/9808015 \[hep-ex\]](#) (cit. on p. 4).
- 119 [5] G. Altarelli et al., *Determination of the Bjorken sum and strong coupling from polarized structure
120 functions*, Nucl. Phys. **B496** (1997) 337, arXiv: [hep-ph/9701289 \[hep-ph\]](#) (cit. on p. 4).
- 121 [6] H. W. Kendall, *Deep inelastic scattering: Experiments on the proton and the observation of scaling*,
122 Rev. Mod. Phys. **63** (3 1991) 597 (cit. on p. 4).
- 123 [7] A. L. Kataev, G. Parente and A. V. Sidorov, *Improved fits to the xF_3 CCFR data at the next-to-next-to-
124 leading order and beyond*, Phys. Part. Nucl. **34** (2003) 20, [Erratum: Phys. Part. Nucl.38,no.6,827(2007)],
125 arXiv: [hep-ph/0106221 \[hep-ph\]](#) (cit. on p. 4).
- 126 [8] S. Alekhin, J. Blumlein and S. Moch, *Parton Distribution Functions and Benchmark Cross Sections at
127 NNLO*, Phys. Rev. D**86** (2012) 054009, arXiv: [1202.2281 \[hep-ph\]](#) (cit. on p. 4).
- 128 [9] S. Alekhin, J. Blumlein and S.-O. Moch, *ABM news and benchmarks*, PoS **DIS2013** (2013) 039, arXiv:
129 [1308.5166 \[hep-ph\]](#) (cit. on p. 4).
- 130 [10] J. Blumlein, H. Bottcher and A. Guffanti, *Non-singlet QCD analysis of deep inelastic world data at
131 $O(\alpha_s^3)$* , Nucl. Phys. **B774** (2007) 182, arXiv: [hep-ph/0607200 \[hep-ph\]](#) (cit. on p. 4).
- 132 [11] H1 Collaboration, *Three- and Four-jet Production at Low x at HERA*, Eur. Phys. J. **C54** (2008) 389,
133 arXiv: [0711.2606 \[hep-ex\]](#) (cit. on p. 4).

- ¹³⁴ [12] ZEUS Collaboration, *Forward-jet production in deep inelastic ep scattering at HERA*, *Eur. Phys. J.* **C52** (2007) 515, arXiv: [0707.3093 \[hep-ex\]](#) (cit. on p. 4).
- ¹³⁵
- ¹³⁶ [13] ZEUS Collaboration, *Multi-jet cross-sections in charged current $e^\pm p$ scattering at HERA*, *Phys. Rev.* **D78** (2008) 032004, arXiv: [0802.3955 \[hep-ex\]](#) (cit. on p. 4).
- ¹³⁷
- ¹³⁸ [14] ZEUS Collaboration, *Inclusive dijet cross sections in neutral current deep inelastic scattering at HERA*, *Eur. Phys. J.* **C70** (2010) 965, arXiv: [1010.6167 \[hep-ex\]](#) (cit. on p. 4).
- ¹³⁹
- ¹⁴⁰ [15] ZEUS Collaboration, *Inclusive-jet cross sections in NC DIS at HERA and a comparison of the kT , anti- kT and SIScone jet algorithms*, *Phys. Lett.* **B691** (2010) 127, arXiv: [1003.2923 \[hep-ex\]](#) (cit. on p. 4).
- ¹⁴¹
- ¹⁴²
- ¹⁴³ [16] H1 Collaboration, *Jet Production in ep Collisions at High Q^2 and Determination of α_s* , *Eur. Phys. J.* **C65** (2010) 363, arXiv: [0904.3870 \[hep-ex\]](#) (cit. on p. 4).
- ¹⁴⁴